

Accepted Manuscript

Evidence for a lava lake on Mt. Michael volcano, Saunders Island (South Sandwich Islands) from Landsat, Sentinel-2 and ASTER satellite imagery

D.M. Gray, A. Burton-Johnson, P.T. Fretwell



PII: S0377-0273(18)30574-2

DOI: <https://doi.org/10.1016/j.jvolgeores.2019.05.002>

Reference: VOLGEO 6603

To appear in: *Journal of Volcanology and Geothermal Research*

Received date: 19 December 2018

Revised date: 1 May 2019

Accepted date: 2 May 2019

Please cite this article as: D.M. Gray, A. Burton-Johnson and P.T. Fretwell, Evidence for a lava lake on Mt. Michael volcano, Saunders Island (South Sandwich Islands) from Landsat, Sentinel-2 and ASTER satellite imagery, *Journal of Volcanology and Geothermal Research*, <https://doi.org/10.1016/j.jvolgeores.2019.05.002>

This is a PDF file of an unedited manuscript that has been accepted for publication. As a service to our customers we are providing this early version of the manuscript. The manuscript will undergo copyediting, typesetting, and review of the resulting proof before it is published in its final form. Please note that during the production process errors may be discovered which could affect the content, and all legal disclaimers that apply to the journal pertain.

Evidence for a lava lake on Mt Michael volcano, Saunders Island (South Sandwich Islands) from Landsat, Sentinel-2 and ASTER satellite imagery

Gray, D.M.^a, Burton-Johnson, A.^{b*}, Fretwell, P.T.^b

^aDepartment of Geography, University College London, Gower Street, London, WC1E 6BT, UK.

^bBritish Antarctic Survey, High Cross, Madingley Road, Cambridge, CB3 0ET, UK

*Author for correspondence

e-mail: alert@bas.ac.uk

Keywords: Remote sensing, volcanology, SWIR, dual-band, Scotia Sea, Antarctica

Highlights (3 points, 85 characters each inc. spaces)

- (1) Mt Michael shows volcanic activity in all suitable satellite images from 1989-2018
- (2) SWIR anomalies image a 110 m (± 40 m) wide lava lake inside the crater from 2003-2018
- (3) Unmixing the SWIR anomalies shows a component of magmatic temperatures (989-1279 °C)

Abstract

Mt. Michael is an active stratovolcano on Saunders Island in the South Sandwich Islands; a remote, oceanic island arc in the southern Atlantic Ocean, bordering the Southern Ocean. The arc contains the only active volcanoes in the South Georgia and South Sandwich Islands British Overseas Territory, yet little is known of their activity. Despite lava lakes being extremely rare with only a few global examples, previous analyses of satellite AVHRR imagery of Mt. Michael in the 1990s showed persistent thermal anomalies not associated with magma overflowing the crater. This suggested the existence of a lava lake inside Mt. Michael's crater. However, their study relied on 1km resolution imagery, and there have been no long-term investigations to determine if this is a persistent feature.

In-situ observations of Mt. Michael are extremely difficult given the location. We used Landsat, Sentinel-2 and ASTER satellite data to monitor activity and detect thermal anomalies within the crater. Persistent volcanic plumes and eruptions were identified throughout the thirty-year period studied. On all 15 occasions that a suitable satellite image was available a thermal anomaly within the crater was detected in the high transmissivity shortwave infrared bands (SWIR) centred on 1.65 μm and 2.2 μm . Pixel-integrated surface temperatures over the crater floor yield temperatures of 284-419 $^{\circ}\text{C}$; comparable to lava lakes elsewhere. Unmixing these temperatures using the dual-band method reveals a molten lava component at basaltic temperatures (989-1279 $^{\circ}\text{C}$) amongst a cooler crust. This is the first evidence for a lava lake within Mt Michael from data that can resolve the crater floor, and the first evidence for magmatic temperatures. As thermal anomalies were detected in all images showing the crater, we suggest that the lava lake is a common and persistent feature.

1. Introduction

[Shortwave and thermal infrared satellite images are examined to determine whether the previously identified lava lake on Mt Michael (South Sandwich Islands) (Lachlan-Cope et al., 2001) is a persistent feature over the last three decades.

1.1 Lava Lakes

Persistent lava lakes are a rare volcanic feature. At any time only a handful of lava lakes have ever been verified globally, and even the most persistent of these cease after 10 to 100 years (Tazieff, 1994). In 'lava pools', ponded lava is triggered by and only persists for the duration of an eruptive episode and are associated with molten lava flowing outside of the crater. In contrast, 'lava lakes' persist beyond a single eruptive episode and are not associated with magma outpourings. Instead, the expelled matter is gaseous and the expelled energy largely thermal (Tazieff, 1994).

Lava lakes are characterised by consistently high thermal anomalies within the volcanic crater, caused by a body of exposed, circulating magma replenished by a reservoir beneath (Harris et al., 1999). Lava lake activity can vary over minutes to decades. Lake levels may fluctuate or drain completely, and the surface can be crusted over or largely molten with violent lava fountains. Surfaces contain both cracks exposing molten lava and larger areas of crust cooled by radiation, heat loss and rainfall (Rothery et al., 1988; Tazieff, 1994).

Volcanoes with persistent lava lakes are less explosive than those without, as volatiles escape freely through the lake (Campion, 2014). This results in emissions solely consisting of gas and thermal energy, rather than magma outpourings. Despite this, their toxic gas emissions encourage regular surveillance.

1.2. Mt Michael, Saunders Island

The South Sandwich Islands (Fig. 1a) are among the world's most active volcanoes, with regular eruptions recorded over the last two centuries (Table 1,

Baker, 1990). The islands are emergent volcanoes, forming a remote 350 km long volcanic arc on the minor (170,000 km²) South Sandwich Plate; overriding the subducting Atlantic Plate. The South Sandwich Plate is bounded to the east by the 8km deep South Sandwich Trench; to the west by the East Scotia Ridge spreading centre; and to the north and south by transcurrent margins. The islands are all relatively small, reaching a maximum of 12 km across. Bristol, Montagu and Saunders Islands, are the largest, and occupy the central portion of the arc.

Mt. Michael is an active basaltic stratovolcano on Saunders Island (57°48' S, 26°28' W). The island and its volcano are largely glaciated except for coastal outcrops and the eroded pyroclastic cones to the east (Fig. 1b & 1c). Fumarole activity has been observed from the 990m high summit crater (Kemp et al., 1931; Baker et al., 1964; Baker, 1990; Lachlan-Cope et al., 2001). Volcanic activity is dominated by effusive or weakly explosive, short-lived Strombolian eruptions, with ejected material limited to a few hundred metres altitude; although extensive lava fields indicate a recent flank eruption (Baker, 1990). The islands were first surveyed in 1931, 156 years after their discovery by Cook (Kemp et al., 1931).

The inaccessibility of Mt Michael and its summit restricts ground observation, requiring the application of remote sensing. Lachlan-Cope et al. (2001) analysed 5000 infrared AVHRR satellite images from 1995-1998. Regular cloud cover restricted observation (only 34 of the 5000 AVHRR images were suitable for analysis, Table 1). Despite this, thermal anomalies not associated with molten lava leaving the crater suggested the existence of an intermittent lava lake within the crater. MODIS satellite data from 2000-2002 also detected a thermal anomaly within Mt. Michael's crater (Table 1, Global Volcanism Program, 2003).

Despite evidence for a lava lake, Lachlan-Cope et al. (2001) could only estimate a uniform temperature due to the 1 km spatial resolution of AVHRR imagery. This was estimated at 350-410 °C, and the lava lake size at 60-160m. Whilst this could resolve a thermal anomaly, it could not resolve the lake itself and prove its presence. To compensate for this, we have analysed three decades of higher-

resolution satellite images to resolve the temperatures within the crater of Mt Michael, and determine whether or not a lava lake is present.

If Mt Michael possesses a persistent lava lake, the associated plumes provide a regular supply of ash, sediment and micronutrients to the ocean (Leat et al., 2013). The constant thermal energy should also prevent extensive ice cover in the crater, reducing the explosivity of the volcano's eruptions (Edwards et al., 2012). Persistent lava lakes are not associated with large-magnitude eruptions due to constant pressure release, but if the lake is intermittent then the island is more hazardous to native species, difficult to predict and poses a greater risk to aircraft than currently assumed.

1.3. Remote sensing of volcanic activity

At certain electromagnetic wavelengths are atmospheric 'windows' through which radiation emitted from the Earth's surface can penetrate. In these regions less than 20% of electromagnetic radiation is absorbed by the atmosphere, allowing the remaining 80% to be transmitted beyond the atmosphere to the altitudes of passive remote sensing satellite systems (i.e. 0.8 transmissivity, Fig. 2; Harris, 2013). Of these high-transmissivity wavelengths, those within the Short Wave Infrared (SWIR, 0.9-3 μm) and Thermal Infrared (TIR, 10-13 μm) are used to monitor volcanoes (Fig. 2). The specific high-transmissivity wavelengths used within these broader spectra are centred on 1.6 and 2.2 μm for SWIR data and 11 μm for TIR data.

Passive satellite remote sensing has been used to monitor active volcanoes since the 1960s, enabling observations in remote, inaccessible locations. Although no satellite missions are specifically designed for this purpose, multiple instruments detect suitable wavelengths. Gawarecki et al. (1965) first applied infrared satellite imagery to volcanic hotspot detection following an eruption at Kilauea. TIR bands have since been used to identify heat signals, plumes and eruptions. NASA's Moderate Resolution Imaging Spectroradiometer (MODIS) is often used for thermal imagery due to its excellent coverage provided by the paired Terra and Aqua satellites and 36 spectral bands. The MODVOLC system uses an algorithm specifically designed to detect high-temperature active lava in MODIS satellite data. It has been successfully employed since 2000 to monitor the

activity of multiple volcanoes globally, including Ambrym, Kilauea and Erta Ale (Wright, 2015). However, the 1 km spatial resolution is too coarse for detailed dual-band analysis of Mt. Michael's 700 m-wide crater. The Advanced Very High Resolution Radiometer (AVHRR) has also been used for volcano monitoring (Lachlan-Cope et al. 2001). The multiple infrared bands enable the dual-band method to be applied, yet detailed analysis at a high resolution over small areas isn't possible, once again due to the 1 km pixel size. NASA's Landsat 3 (launched in 1978) provided TIR images at 120 m resolution, refined in successive missions to 100 m for Landsat 8 (launched in 2013).

Inconclusive satellite TIR analysis encouraged application of satellite SWIR data to volcanic observation (Wiesnet and D'Aguanno, 1982; Rothery et al., 1988). Unlike TIR, SWIR satellite imagery has sufficient spatial resolution to detect small hotspots (<20m). Differing temperatures between two SWIR bands for the same pixel indicates the pixel contains at least two different temperatures (Harris, 2013). A temperature calculated for the pixel using the Planck equation is thus a 'pixel-integrated temperature': a weighted combination of two temperatures. The dual-band method of Dozier (1981) uses two different wavelengths to unmix this pixel-integrated temperature and allow estimation of both temperatures and the fraction of the pixel occupied by the two surfaces.

This utilisation of two bands gives SWIR an advantage over TIR data. Many TIR studies have used Landsat and AVHRR data, yet the spatial resolution on the latter is too coarse to resolve details within volcanic craters and Landsat 8's second thermal band is impacted by stray light. SWIR bands on Landsat, Sentinel and ASTER instruments do not have this problem. Landsat and ASTER SWIR data and the dual-band method have been used extensively for hotspot detection, including studies of Mt. Erebus, Erta 'Ale and Lascar volcano in Chile (Rothery et al., 1988; Rothery and Oppenheimer, 1994; Harris et al., 1999, Blackett, 2013).

2. Methodology

The methodology applied here comprises multiple steps, starting with data acquisition. The workflow is summarised in Fig. 3.

2.1. Data acquisition

This study utilised the freely available data from Landsat missions 4 to 8 (NASA), Sentinel-2 (ESA), and the ASTER sensor of the Terra satellite (NASA). These offer SWIR resolutions of 30 m (Landsat and ASTER) and 10 m (Sentinel-2), and TIR resolutions of 90 m (ASTER), 60m (Landsat 7), and 100 m (Landsat 8). Whilst other satellites carry multispectral infrared instruments, few are suitable for this investigation. NASA's Moderate Resolution Imaging Spectroradiometer (MODIS) is often used for thermal imagery due to its excellent coverage and 36 spectral bands. However, the 1 km spatial resolution is too coarse to resolve details inside the crater of Mt Michael. The multiple infrared bands of the Advanced Very High Resolution Radiometer (AVHRR) (used by Lachlan-Cope et al., 2001) also have a 1 km pixel size. The commercial satellites, IKONOS and Quickbird, do not have the necessary infrared bands. Consequently, Landsat, Sentinel-2 and ASTER offer the best solutions for this study.

2.2. Image pre-processing

Level 1 Landsat, Sentinel and ASTER images that did not contain 100% cloud cover were downloaded and imported into ArcMap as raster layers. Any images in which the island is obscured by cloud were discarded. For the remaining images, the red and two SWIR bands for each date were combined to create a false colour image which emphasises any thermal anomaly in blue (Fig. 7a).

Where a thermal anomaly was identified, the spectral radiance and equivalent temperatures of the anomalous pixels was obtained through SWIR analysis using GIS and Python. All images were first converted from the distributed data format (Q_{cal}) to top of atmosphere radiance (L_λ , $W\ m^{-2}\ sr^{-1}\ \mu m^{-1}$). For Landsat images, radiance is calculated as:

$$L_\lambda = M_L Q_{cal} + A_L$$

Eq. 1.

Sentinel images are converted to radiance by:

$$L_\lambda = \frac{Q_{cal} E_{e\lambda}(\cos\theta)}{\pi \left(\frac{1}{U}\right)} / 10^4$$

Eq. 2.

And ASTER images were converted according to:

$$L_{\lambda} = (Q_{cal} - 1) * gain_{\lambda}$$

Eq. 3.

Where M_L = multiplicative rescaling factor; A_L = additive rescaling factor; Q_{cal} = digital number (DN), $E_{e\lambda}$ = solar irradiance; θ = incidence angle; U = quantification value, and $gain_{\lambda}$ = the gain for that image at wavelength λ . All parameters given in Tables 2 to 4.

2.3. Blackbody temperature calculation

Infrared remote sensing of volcanic activity uses the Planck Function to calculate spectral radiance emitted by a blackbody at a given temperature and wavelength. The higher the temperature, the greater the radiance. A blackbody is a hypothetical surface absorbing all received radiation and reflecting none. The energy absorbed heats the blackbody, which then radiates energy with a temperature-defined spectrum and perfect emissivity ($\varepsilon = 1$). Blackbodies are assumed to emit radiation isotropically (in all directions) and thus emitted energy is evenly distributed above the Earth's surface. As temperature increases, the wavelength of peak spectral radiance decreases (Fig. 4). This is described by Wein's Displacement Law (Eq. 4), where T is the temperature corresponding to the wavelength (λ) at which the blackbody curve peaks, and A is Wein's constant (2898 μm).

$$\lambda = A/T$$

Eq. 4.

At ambient temperatures, very little radiance is detected in SWIR and is greatest in TIR (Fig. 5). As temperature increases, spectral radiance also increases but at a higher rate for shorter infrared wavelengths (Fig. 5; Harris, 2013). Thus, at temperatures above 300 °C, radiance is higher in SWIR than TIR (Fig. 5). Lava lake temperatures range from approximately 200°C for the crust to 1200°C for molten lava (Rothery et al., 1988; Tazieff, 1994). The equivalent temperatures recorded across an entire pixel (290 to 420 °C) coincide with the detectable range in SWIR: 100-320 °C for 2.2 μm and 225-420 °C for 1.65 μm (Francis and Rothery, 1987; Rothery et al., 1988). These wavelengths are thus ideal for

analysing volcanic thermal anomalies that would be saturated or undetectable in TIR (Blackett, 2017).

If the spectral radiance and wavelength are known, the Planck Function can be solved for blackbody temperature (T , Eq. 5, adapted from Francis and Rothery, 1987; Rothery et al., 1988; Harris, 2013). The blackbody is idealised, as all natural surfaces on Earth are grey-bodies reflecting a small amount of incident radiation (Harris, 2013), and thus reradiating less than 100% of the incident energy (Campbell and Wynne, 2011). Spectral radiance reaching the satellite sensor is also reduced due to atmospheric attenuation and absorption by gases. Eq. 5 can thus be adjusted to include emissivity and transmissivity (Eq. 6).

$$T = \frac{c_2}{\lambda \ln([\varepsilon c_1 \lambda^{-5} / 10^6 \pi L_\lambda] + 1)}$$

Eq. 5.

$$T = \frac{c_2}{\lambda \ln([\varepsilon \tau c_1 \lambda^{-5} / 10^6 \pi L_\lambda] + 1)}$$

Eq. 6.

Where: L_λ = radiance ($\text{W m}^{-2} \text{sr}^{-1} \mu\text{m}^{-1}$); $c_1 = 3.742 \times 10^{-16}$ (W m^2); $c_2 = 0.0144$ (m K); λ = wavelength (m); T = blackbody temperature (K); ε = emissivity of the radiating surface; and τ = atmospheric transmission. c_1 and c_2 are simplified constants representing hc^2 and hc/k , where h is Planck's constant (6.266×10^{-34} J s), c is speed of light (2.998×10^8 m s $^{-1}$) and k is Boltzmann's constant ($2987 \mu\text{m K}$).

2.4. The dual-band method

The calculated blackbody temperatures are maximum 'pixel-integrated temperatures' and assume that the surface has a uniform temperature. This temperature can be unmixed into two components using the dual-band method (Dozier, 1981). If two wavelengths record different temperatures for the same pixel location, this indicates a weighted combination of two temperatures (providing the wavelengths are suitably far apart). Given that spectral radiance at high temperatures increases at shorter wavelengths, a much greater portion of the total radiance from molten lava will be detectable in SWIR than longer wavelengths. This is why pixel-integrated temperatures change with wavelength.

Consider a single 30 m pixel covering part of a lava lake. The pixel likely consists of multiple surface components and temperature varies over mm to cm spatial scales (Harris, 2013). The temperature of heavily crusted lava will be of a significantly lower temperature than any cracks of molten lava, but if the crust occupies more surface area than cracks, the pixel-integrated temperature will be skewed towards the lower temperature of the former. The pixel-integrated temperature for 99% crust at 200 °C and 1% molten lava at 1200 °C will be approximately 250 °C In Landsat TM band 7 (~2.2 µm) and 400 °C in band 5 (~1.65 µm). The pixel-integrated values thus do not represent the individual temperature components and must be unmixed.

The dual-band method requires solving a pair of simultaneous equations (Eq. 7 and 8) with three unknowns: the cool temperature (T_c), hot temperature (T_h) and fraction of the pixel occupied by one of these (f_c or f_h).

$$L(T_x\lambda_x) = \varepsilon_x\tau_x[f_hL(T_h\lambda_x) + (1 - f_h)L(T_c\lambda_x)]$$

Eq. 7.

$$L(T_y\lambda_y) = \varepsilon_y\tau_y[f_hL(T_h\lambda_y) + (1 - f_h)L(T_c\lambda_y)]$$

Eq. 8.

Where L is the blackbody spectral radiance for a given temperature (T) and wavelength (λ), ε is emissivity of the radiating surface, τ is atmospheric transmission, T_x and T_y are the pixel-integrated temperatures in bands x and y (Lombardo et al., 2012).

At least one variable must be estimated or measured, allowing the remaining two to be solved numerically or graphically. For Mt Michael, the most radiant pixel was chosen for dual-band analysis. Although the size of the thermal anomaly within the crater varied between 90-215 m across, the percentage of the most radiant pixel occupied by molten lava did not exceed 0.57%, validating the use of a single pixel for these calculations. Other, less radiant pixels within the anomaly were assumed to represent mostly crusted lava and crater wall or floor. As the pixel sizes for all satellites used are small at 10-30 m, we assume the most radiant pixel contains only two components: The cool temperature corresponds with the cooler crust of the lava lake (T_c) and the hot temperature that of the

molten lava (T_h). Using published values (Rothery et al., 1988) the crust was estimated at 200 °C. The two variables to be solved were T_h and the fraction of the pixel it occupied (f_h). This is solved graphically as for each wavelength T_h and f_h are non-unique, but the intersection of the two plots is a unique solution (Fig. 6).

Emissivity and atmospheric transmission were also estimated. Emissivity (ϵ) is the ratio of radiance emitted by a surface to that emitted by a perfect blackbody at the same given temperature and wavelength (Li et al., 2012). ϵ ranges from 0 to 1, where 1 represents a perfect blackbody. As ϵ for basaltic surfaces varies slightly with wavelength it is a selective radiator rather than a blackbody, and thus ϵ is dependent on the wavelengths analysed (Harris, 2013). In previous studies, ϵ ranges from 0.6 to 0.99 depending on the temperature and exact mineral composition of the lava (Rothery et al., 1988; Harris et al., 1999; Murphy et al., 2011; Blackett, 2017). Inside Mt. Michael's crater, ϵ was estimated by reducing the value from 0.9 to 0.8 in 0.02 increments until the upper and lower temperature limits ($T_c = 200$ °C; $T_h = 1200$ °C, the approximate temperature of molten basaltic lava) were not exceeded. The Landsat 8 image acquired on 31-Jan-2018 was used as it had visibly low attenuation and saturation (Fig. 7a). The resultant value of ϵ was 0.8; similar to that used for SWIR data at Lascar volcano (0.8; Francis and Rothery, 1987) and Erta 'Ale (0.74; Burgi et al., 2002).

MODTRAN was used to calculate atmospheric transmission using radiative transfer theory (Berk et al., 2014). This describes how electromagnetic radiation transfers energy through a medium considering the effects of scattering, absorption and emission (Jensen, 2007). There are no atmospheric models for sub-Antarctic latitudes (46-60 °S) so sub-Arctic winter and sub-Arctic summer (50-70 °N) models were used. Corresponding ground temperatures were changed to the South Sandwich Islands summer and winter averages: 281 K and 267 K. The navy aerosol model was used to define the meteorological range from the ground to 2 km altitude. Default parameters for wind speed and visibility were left unchanged and the maximum possible sensor altitude was used (99 km). Albedo was set to 0, representing the albedo inside the volcano's crater rather than its flanks. Calculated transmissivities are detailed in Table 5 and the

spectrum in Fig. 2. We used the mean of the average transmissivities for each central SWIR wavelength: 0.9.

With the parameters defined, the dual-band simultaneous equations were solved graphically at intervals of 50 °C, with the precise intersect value (e.g. Fig. 6) determined using Python (<https://github.com/dmgrayuk/mtmichaelvolcano>).

2.5. Identifying volcanic plumes

Where no clear heat signal was displayed, images were reviewed for other signs of volcanic activity. When volcanic plumes ascend above local cloud cover they appear either lighter or darker than the surrounding cloud, depending on the wavelength used: Brighter in SWIR (Fig. 7b), and darker in TIR (Fig. 7c). For visually inconclusive images, two TIR bands were used to calculate the brightness temperature difference (BTD; Fig. 7d). This involves calculating the top of atmosphere radiance for each TIR band, converting this to brightness temperature (BT; Eq. 8), then subtracting the BT of the longer from the shorter band. If the BTD is <-0.4 this suggests volcanic rather than meteorological clouds, although the strength of the signal can vary (Webley et al., 2012). Brightness temperature is calculated as:

$$BT = \frac{K_2}{\ln\left(\frac{K_1}{L_\lambda + 1}\right)}$$

Eq. 9.

Where K_1 and K_2 are the first and second thermal conversion constants found in the metadata for each TIR band.

2.6. Methodological uncertainty

2.6.1. Assumed values

The dual-band method requires estimation of one of three unknown variables (T_h , T_c and F_h). These values are difficult to constrain and vary between lava lakes (Lombardo et al., 2012). The assumed T_c (200 °C) is reasonable based on published values (Rothery et al., 1988). For the two clearest images, the corresponding T_h (1040-1200°C) and F_h (0.0017-0.0024) are comparable to Lascar volcano, Ert'a Ale and Mt. Erebus (Rothery et al., 1988). In-situ

measurements elsewhere indicate T_h is less variable and easier to constrain than T_c (Le Guern et al., 1979; Flynn, 1992). However, fixing this variable at 1200 °C and solving for T_c at Mt Michael, some equations remain unsolvable as F_h is <0.0001 or the calculated T_c is unrealistically low. This suggests one of the assumed values or the assumptions of what T_c and T_h represent are incorrect; the surface of the lake could be entirely crusted over in these instances or T_h could be crusted lava and T_c cold crater floor. Alternatively, a two-component model is unsuitable for a pixel that may contain more components (Harris, 2013). Lava lake surfaces are highly variable over small spatial scales ($<30\text{m}$) and pixels away from the lake centre could contain cracks of molten lava, hot crustal lava, and cooler accumulated crust and debris (Harris, 2013). Studies have shown that in these instances using three components or three spectral bands may be more effective (Harris et al., 1999; Oppenheimer, 1993).

Errors are also introduced through the selection of an effective wavelength in each band for use in the equations. The central wavelength of each band was used for all our calculations. The ranges are relatively small, but can still give errors up to 10 K for pixel-integrated temperatures and 30 K in dual-band calculations (Rothery et al., 1988).

2.6.2. Emissivity

As discussed, the emissivity was estimated at 0.8 based on iterative calculations. However, this value will increase as fresh lava solidifies; decreasing its reflectance (Harris, 2013). Consequently, emissivity in an active lava lake will change within a pixel and between scenes. The impact is small, as Rothery et al. (1988) show that an emissivity uncertainty of ± 0.2 gives pixel-integrated temperature errors of ± 15 K, and our findings suggest an uncertainty of ± 0.1 gives T_h errors of ± 15 K. Depending on the mineralogy, temperature and wavelength of an observation, the emissivity of lava lakes range from 0.6-0.99, is lower at shorter wavelengths, and is unlikely to fall below 0.5 in SWIR (Rothery et al., 1988; Harris et al., 1999; Murphy et al., 2011; Harris, 2013; Blackett, 2017). This implies a maximum pixel-integrated temperature error of ± 30 K and dual-band T_h error of ± 60 K. Values >0.8 yield unrealistically high T_h estimates. Reducing the potential range to 0.6-0.8 gives a T_h error of ± 30 K. This difficulty in

calculating SWIR emissivity leads many volcanic activity studies to assume a value (e.g. Rothery et al., 1988; Murphy et al., 2011, Blackett, 2017).

2.6.3. Transmissivity

As discussed, transmissivity was estimated as 0.9 using MODTRAN. This method requires multiple assumptions and knowledge of land surface and atmospheric conditions. A temperature uncertainty of ± 1 K yields a transmissivity error of ± 0.006 . Changing the albedo from 0 to 1 results in a change of 0.008. Given the temperature variability in the South Sandwich Islands (Baker et al., 1964) the maximum error is ± 0.0152 . This equates to a pixel-integrated temperature error of ± 0.75 K, although Lombardo et al. (2012) indicate that for T_h this is ~ 3.6 K.

MODTRAN is unable to consider the volume of volcanic gaseous emissions, the effects of which are largely unknown. Small accumulations of steam or vapour within the crater can increase radiation absorption (Oppenheimer, 1991; Harris et al., 1999). A transmissivity of 0.9 is thus likely an overestimate during periods of high emissions. However, in this scenario it would be difficult to obtain a reliable pixel-integrated temperature or to perform dual-band calculations. Thus when the observed thermal anomaly only covers a few pixels this reflects low gaseous emissions. The error in transmissivity is then minimal and consequent errors for a ± 0.2 uncertainty are $< \pm 20$ K for a pixel-integrated temperature or $< \pm 48$ K for the dual-band T_h .

Propagating the quantified errors for effective wavelength, emissivity, and transmissivity predicts ± 27 K uncertainty for the pixel-integrated temperatures and ± 64 K for the dual-band method (Currell, 2015).

2.6.4. Radiometric Uncertainty

Each satellite has a radiometric uncertainty in the accuracy of at-sensor radiance measurements. For Landsat 7 and ASTER this is 4% (Duda et al., 2015; Zanter, 2019), reducing to 5-3% for Sentinel-2 and 3% for Landsat 8 (SUHET, 2015; Zanter, 2019). This equates to approximately ± 0.001 μm . As the wavelengths used were measured to the nearest 0.01 μm , this error is negligible.

3. Results

3.1 Data acquisition

Over the thirty years studied, only 115 images were not obscured by atmospheric clouds (Table 6). Seasonal variations in cloud cover bias the data towards the clearer conditions of summer months (70% of images analysed are from October-March). The number of images was also reduced by the acquisition history of the satellite data. Sentinel-2 has only been operational since 2015 and Saunders Island is only covered since 2018. There are notable gaps in Landsat data and many 12-month periods are represented by only 1 or 2 images, rather than the 40+ possible from the satellite's ~8-day mid-latitude revisit period. In November 2013, Landsat 7 ceased to capture images of Antarctica, Greenland and oceanic islands. Landsat 8 started to acquire these areas soon after its launch, but data is only available from 2015. No Landsat data is available for the South Sandwich Islands prior to 1983 due to coverage and the incomplete assimilation and loss of ground station data (Wulder et al., 2016).

3.2. Data Quality

Data quality is variable throughout the thirty-year period investigated. This is due to radiometric quality, sensor saturation, and instrument failure. Technological advancement improved the signal to noise ratio and resolution of Landsat 8 and Sentinel-2 imagery compared to Landsat 4. In addition to data loss through pixel saturation, data loss was caused by the breakdown of the Scan Line Corrector (SLC) on Landsat 7's Enhanced Thematic Mapper Plus (ETM+), resulting in linear gaps (stripes) across subsequent images and possible loss of higher temperature pixels (e.g. Fig. 9a and 8c).

3.3. Evidence of Volcanic Activity

We characterise volcanic activity as: a) plumes, where emissions are not associated with explosive activity but rather degassing of the lava lake (Fig. 8a); b) volcanic clouds, where emissions are dispersed into the atmosphere (Fig. 8b); c) Strombolian eruptions, where larger plumes are associated with explosive

activity (Fig. 8c); and d) possible evidence for a lava lake, where a clear thermal anomaly is detected in the crater (Fig. 8d). We also recorded the occurrence of TIR thermal anomalies without evidence in the SWIR. Of the 115 images not obscured by cloud, 100% show evidence of volcanic activity (Table 6). This agrees with 200 years of reported sightings of a permanent plume emanating from the crater (Holdgate and Baker, 1979; Patrick and Smellie, 2013).

Only 15 images display both a strong SWIR thermal anomaly and a view of the summit region (albeit with the crater floor obscured by plumes in all but 7 images, Fig. 9). These give maximum pixel-integrated temperatures (Fig. 10, Table 7) of 331-570 °C and 228-376 °C for the two SWIR bands (1.61-1.65 μm and 2.19-2.2 μm , respectively). Using the dual-band method, a second hot component (T_h) was calculated in addition to an assumed cooler component (T_c , 200 °C). T_h varies between 989-1279 °C (± 64 °C; Fig. 11, Table 8) and forms 0.03-0.57 % of the pixels analysed. The hottest pixels in three of the images (Fig. 9a, 9b, 9e) may have been removed due to the Scan Line Corrector failure (i.e. the linear data gaps) so it is possible T_h and F_h vary more than the values obtained here.

4. Discussion

Every satellite image analysed shows volcanic activity, with the volcano exhibiting an apparently constant plume. However, this plume obscures the floor of the crater in all but five images. Despite the high transmissivity of the SWIR wavelengths used (Fig. 2), these volcanic emissions diffuse the thermal signal from the crater, emit their own energy, and increase the albedo of the pixels (Fig. 9). Consequently, the lack of a diffuse thermal signal in the night-time ASTER image (13/07/2005, Fig. 9c) also indicates a clear view of the crater.

All images with a clear view of the crater exhibit SWIR thermal anomalies 90-215 m wide in the crater floor (Fig. 9c, e, f, j, l, and m). The dimensions of these anomalies allow a best estimate of the lava lake width of 110 m (± 40 m, 1SD) and a lake area of 0.01 km² (± 0.003 km², 1SD). The mean pixel-integrated temperatures for the SWIR bands give temperatures of 331-505 °C (1.61-1.65 μm) and 237-333 °C (2.19-2.2 μm) for the warmest pixel in these anomalies

(mean for both bands of 284-419 °C, Fig. 10). These temperatures are reasonable for a lava lake with a large area of cooled crust and small cracks of molten lava (Rothery et al., 1988), and are similar to those of Lachlan-Cope et al. (2001). However, unlike their AVHRR data, this higher-resolution data is able to resolve the crater floor and show temperatures expected for lava lake behaviour within the volcano crater.

Even so, these pixel-integrated temperatures do not prove the presence of liquid magma (as required for a lava lake), and consequently the dual-band method was applied. Of the 15 images for which SWIR pixel-integrated temperatures could be determined (Fig. 9), 7 were solvable by the dual-band method (Fig. 11). The method broke down when applied to the remaining 8 as F_h was <0.0001 . This could indicate the presence of an entirely crusted over lava lake and thus just one thermal component within the pixel, rather than the assumed two. T_h for these images (989-1279 °C) corresponds with magmatic temperatures, indicating liquid magma is generating the elevated pixel-integrated temperatures. The proportion of each pixel occupied by these magmatic temperatures (f_h , 0.02-0.17 %) indicates the presence of cracks of liquid magma between much larger areas of 200 °C crust; evidence for a lava lake within Mt Michael.

The temperature variations in both methods may result from: partial covering of the lake's surface from erupted ejecta or rock fall within the crater; varying lake circulation; or volcanic cloud and gaseous emissions obscuring the lake (Flynn et al., 1993; Lachlan-Cope et al., 2001). Another explanation could be fluctuating levels in the lake, indicated not only by temperature change but also the variable emission of volcanic plumes within the crater (Patrick and Smellie, 2013). However, it is difficult to differentiate between a small lava lake with frequent overflows of molten lava onto the surrounding crater floor and a larger lava lake, as both could emit similar radiances and fluctuate in both size and temperature.

The calculated values and observed behaviour are comparable to the lava lakes of Ambrym volcano in the Vanuatu arc, characterised by regular, low-magnitude Strombolian eruptions and passive degassing at all other times (Firth et al., 2016). However, Ambrym's lakes are very active with a large volume of molten

lava constantly exposed, whereas Mt. Michael's lake is likely to have a higher proportion of surface crust (Allard et al. 2016); the proportion of crust at Mt Michael is more similar to Mt. Erebus, Antarctica (Murphy et al., 2011). The observed molten lava temperatures (T_h) are comparable to those of the Lascar volcano's lava lake, Chile (Rothery et al., 1988).

Although the crater floor is covered by plumes in most of the 15 images of the crater (Fig. 9), magmatic values for T_h are also evidenced in dual-band analyses of images where the crater floor was obscured. This indicates that although the SWIR pixel-integrated temperatures are diffused by the plumes (Fig. 9) the maximum values still reflect the magmatic temperature of a lava lake on crater floor; a result of the high transmissivities of these specific SWIR wavelengths (Fig. 2). Despite being a small data set, as magmatic temperatures can be determined for 100% of these images over a 15 year period the lava lake may be a persistent feature.

5. Conclusions

From 1989-2018, all satellite images of Mt Michael show evidence for volcanic activity. Shortwave infrared (SWIR) data give pixel-integrated temperatures within the crater of Mt Michael of 284-473 °C (± 27 °C). When images are clear of volcanic emissions, these warm pixels cover a 90-215 m wide anomaly on the crater floor. Dual-band analyses of the SWIR data show the presence of two components: a warm crust covering most of the pixel and a much less extensive component with magmatic temperatures (989-1279 °C). Both methods of SWIR analyses give results similar to known lava lakes elsewhere. The presence of comparable anomalies and temperatures within the crater floor of Mt Michael in the absence of eruptive activity indicates the presence of a persistent lava lake over the period studied. Although temperature anomalies had been detected over Mt Michael previously, this is the first time the lava lake and its magmatic temperatures have been resolved.

6. Acknowledgements

This research was conducted for an MSc Thesis at University College London, and we thank the University for its support. We also thank our Editor, Diana Roman, and our reviewers, Brett Carr and an anonymous reviewer, for helping us improve the manuscript.

7. References

- Amante, C., Eakins, B.W., 2009. ETOPO1 Arc-Minute Global Relief Model: Procedures, Data Sources and Analysis, National Oceanic and Atmospheric Administration Technical Memorandum NESDIS NGDC-24.
- Baker, P.E., 1990. South Sandwich Islands. In: LeMasurier, W.E., Thomson, J.W. (Eds.), *Volcanoes of the Antarctic Plate and Southern Oceans*, Antarctic Research Series. American Geophysical Union, 361–395.
- Baker, P.E., Holdgate, M.W., Longton, R.E., Tilbrook, P.J., Tomblin, J.F., Vaughan, R.W., Wynne-Edwards, C.J.C., 1964. A survey of the South Sandwich Islands. *Nature* 203, 691.
- Berk, A., Conforti, P., Kennett, R., Perkins, T., Hawes, F., van den Bosch, J., 2014. MODTRAN6: a major upgrade of the MODTRAN radiative transfer code. *Proceedings SPIE 9088, Algorithms and Technologies for Multispectral, Hyperspectral, and Ultraspectral Imagery XX*.
- Blackett, M., 2013. Review of the utility of infrared remote sensing for detecting and monitoring volcanic activity with the case study of shortwave infrared data for Lascar Volcano from 2001-2005. Geological Society, London, Special Publications, 107-135.
- Blackett, M., 2017. An overview of infrared remote sensing of volcanic activity. *Journal of Imaging* 3, 13.
- Burgi, P.-Y., Caillet, M., Haefeli, S., 2002. Field temperature measurements at Erta'Ale lava lake, Ethiopia. *Bulletin of Volcanology* 64, 472–485.
- Campbell, J.B., Wynne, R.H., 2011. *Introduction to remote sensing*, 5th Edition. ed. Guilford Press, New York, USA.
- Campion, R., 2014. New lava lake at Nyamuragira volcano revealed by combined ASTER and OMI SO₂ measurements. *Geophysical Research Letters* 41, 7485–7492.
- Currell, G., 2015. *Scientific data analysis*. Oxford University Press, Oxford, UK.
- Dozier, J., 1981. A method for satellite identification of surface temperature fields of subpixel resolution. *Remote Sensing of Environment* 11, 221–229.

Duda, K., Daucsavage, J., Siemonsma, D., Brooks, B., Oleson, R., Meyer, D., Doescher, C., 2015. Advanced Spaceborne Thermal Emission and Reflection Radiometer (ASTER) Level 1 Precision Terrain Corrected Registered At-Sensor Radiance Product (AST_L1T) - AST_L1T Product User's Guide. Department of the Interior, U.S. Geological Survey, Sioux Falls, South Dakota, USA.

Edwards, B., Magnússon, E., Thordarson, T., Guðmundsson, M.T., Höskuldsson, A., Oddsson, B., Haklar, J., 2012. Interactions between lava and snow/ice during the 2010 Fimmvörðuháls eruption, south-central Iceland. *Journal of Geophysical Research: Solid Earth* 117.

Firth, C., Handley, H., Turner, S., Cronin, S., Smith, I., 2016. Variable conditions of magma storage and differentiation with links to eruption style at Ambrym Volcano, Vanuatu. *Journal of Petrology* 57, 1049–1072.

Flynn, L.P., 1992. Radiative temperature measurements of the Pu'u 'O'o-Kupaianaha eruption with implications for satellite remote sensing. PhD Thesis. Department of Geology and Geography, University of Hawaii, Manoa.

Flynn, L.P., Mouginis-Mark, P.J., Gradie, J.C., Lucey, P.G., 1993. Radiative temperature measurements at Kupaianaha lava lake, Kilauea Volcano, Hawaii. *Journal of Geophysical Research: Solid Earth* 98, 6461–6476.

Francis, P.W., Rothery, D.A., 1987. Using the Landsat Thematic Mapper to detect and monitor active volcanoes: An example from Lascar volcano, northern Chile. *Geology* 15, 614–617.

Gawarecki, S.J., Lyon, R.J.P., Nordberg, W., 1965. Infrared spectral returns and imagery of the earth from space and their application to geologic problems. In: Badgley, P.C. (Ed.), AAS Science and Technology Series. Presented at the Scientific experiments for manned orbital flight, proceedings of the third Goddard Memorial Symposium, American Astronautical Society, Washington, D.C., USA, 10–30.

Global Volcanism Program, 2003. Report on Saunders (United Kingdom). In: Venzke, E. (Ed.), Bulletin of the Global Volcanism Network. Smithsonian Institution, Washington, D.C., USA.

- Harris, A., 2013. Thermal remote sensing of active volcanoes: a user's manual. Cambridge University Press, Cambridge, UK.
- Harris, A.J., Flynn, L.P., Rothery, D.A., Oppenheimer, C., Sherman, S.B., 1999. Mass flux measurements at active lava lakes: implications for magma recycling. *Journal of Geophysical Research: Solid Earth* 104, 7117–7136.
- Holdgate, M.W., Baker, P.E., 1979. The South Sandwich Islands: I. General Description. *British Antarctic Survey Scientific Reports* 91.
- Jensen, J.R., 2007. Remote sensing of the environment: an earth resource perspective: Pearson Prentice Hall. Upper Saddle River, NJ.
- Kemp, S., NELSON, A.L., Tyrrell, G.W., 1931. The South Sandwich Islands... With a Report on Rock Specimens by GW Tyrrell.
- Lachlan-Cope, T., Smellie, J.L., Ladkin, R., 2001. Discovery of a recurrent lava lake on Saunders Island (South Sandwich Islands) using AVHRR imagery. *Journal of Volcanology and Geothermal Research* 112, 105–116.
- Le Guern, F., Carbonnelle, J., Tazieff, H., 1979. Erta'Ale lava lake: heat and gas transfer to the atmosphere. *Journal of Volcanology and Geothermal Research* 6, 27–48.
- Leat, P.T., Day, S.J., Tate, A.J., Martin, T.J., Owen, M.J., Tappin, D.R., 2013. Volcanic evolution of the South Sandwich volcanic arc, South Atlantic, from multibeam bathymetry. *Journal of Volcanology and Geothermal Research* 265, 60–77.
- Li, Z., Li, J., Li, Y., Zhang, Y., Schmit, T.J., Zhou, L., Goldberg, M.D., Menzel, W.P., 2012. Determining diurnal variations of land surface emissivity from geostationary satellites. *Journal of Geophysical Research: Atmospheres* 117.
- Lombardo, V., Musacchio, M., Buongiorno, M.F., 2012. Error analysis of subpixel lava temperature measurements using infrared remotely sensed data. *Geophysical Journal International* 191, 112–125.
- Murphy, S.W., de Souza Filho, C.R., Oppenheimer, C., 2011. Monitoring volcanic thermal anomalies from space: Size matters. *Journal of Volcanology and Geothermal Research* 203, 48–61.

Oppenheimer, C., 1991. Lava flow cooling estimated from Landsat Thematic Mapper infrared data: the Lonquimay eruption (Chile, 1989). *Journal of Geophysical Research: Solid Earth* 96, 21865–21878.

Oppenheimer, C., 1993. Thermal distributions of hot volcanic surfaces constrained using three infrared bands of remote sensing data. *Geophysical Research Letters* 20 (6), 431–434

Patrick, M.R., Smellie, J.L., 2013. Synthesis A spaceborne inventory of volcanic activity in Antarctica and southern oceans, 2000–10. *Antarctic Science* 25, 475–500.

Rothery, D.A., Francis, P.W., Wood, C.A., 1988. Volcano monitoring using short wavelength infrared data from satellites. *Journal of Geophysical Research: Solid Earth* 93, 7993–8008.

Rothery, D.A., Oppenheimer, C., 1994. Monitoring Mount Erebus by satellite remote sensing. *Volcanological and Environmental Studies of Mount Erebus, Antarctica* 51–56.

SUHET, 2015. Sentinel-2 User Handbook. No. Issue 1, Revision 2, ESA Standard Document. European Space Agency.

Tazieff, H., 1994. Permanent lava lakes: observed facts and induced mechanisms. *Journal of Volcanology and Geothermal Research* 63, 3–11.

Webley, P.W., Steensen, T., Stuefer, M., Grell, G., Freitas, S., Pavolonis, M., 2012. Analyzing the Eyjafjallajökull 2010 eruption using satellite remote sensing, lidar and WRF-Chem dispersion and tracking model. *Journal of Geophysical Research: Atmospheres* 117.

Wiesnet, D.R., D'Aguianno, J., 1982. Thermal imagery of Mount Erebus from the NOAA-6 satellite. *Antarctic Journal of the United States* 17, 32–34.

Wright, R., 2015. MODVOLC: 14 years of autonomous observations of effusive volcanism from space. Geological Society, London, Special Publications, 426, 23–27.

Wulder, M.A., White, J.C., Loveland, T.R., Woodcock, C.E., Belward, A.S., Cohen, W.B., Fosnight, E.A., Shaw, J., Masek, J.G., Roy, D.P., 2016. The global Landsat

archive: Status, consolidation, and direction. Remote Sensing of Environment 185, 271–283.

Zanter, K., 2019. Landsat Collection 1 Level 1 Product Definition. Department of the Interior, U.S. Geological Survey, Sioux Falls, South Dakota, USA.

Figure Captions

Fig. 1. a) Regional map of the Scotia Sea and South Sandwich Islands. Bathymetry from ETOPO1 (Amante and Eakins, 2009). b) Aerial photograph of Mt Michael summit (01/1997), photo courtesy of Pete Bucktrout (British Antarctic Survey). c) Sentinel-2 RGB image of Saunders Island (10/02/2018).

Fig. 2. Calculated transmissivity spectrum from MODTRAN used for this study (Berk et al., 2014).

Fig. 3. Flowchart of this study's workflow for satellite image analysis.

Fig. 4. Variation of blackbody spectral radiance with temperature (adapted from Blackett, 2017).

Fig. 5. Relationship between blackbody temperature and spectral radiance for the SWIR (1.65 and 2.2 μm) and TIR (11 μm).

Fig. 6. Example of a unique graphical solution (red dot) for T_h and f_h using the dual-band method of SWIR temperature analysis.

Fig. 7. Identifying volcanic activity from Landsat 8 TIR and SWIR imagery. Outline of Saunders Island is shown in red. a) False colour image (red and two SWIR bands) of Mt Michael, 31.01.2018. SWIR thermal anomaly evidenced by the blue pixels. b) Eruption from Mt. Michael visible in the SWIR as a lighter, white plume compared to surrounding cloud, 11.12.2016. c) Eruption from Mt. Michael visible in the TIR as a dark plume, 11.12.2016. d) Brightness temperature difference (BTD) image showing an eruption from Mt. Michael visible as a darker plume against the surrounding cloud, 11.12.2016.

Fig. 8. Categories of observed volcanic activity used in this study. Outline of Saunders Island is shown in red: a) Plume (Landsat 8, 21.08.2016), b) volcanic cloud shown in yellow box (Landsat 4, 24.02.1989), c) Strombolian eruption (Landsat 7, 29.11.2006), and d) possible lava lake (Landsat 8, 31.01.2018).

Fig. 9. Pixel-integrated temperatures for all 15 images showing the crater of Mt Michael, overlain on data from the blue (ASTER and Sentinel-2) or panchromatic (Landsat) bands. Image c) was taken at night, so in the absence of visible imagery is overlain on TIR data.

Fig. 10. Pixel-integrated temperatures from the two SWIR bands for the warmest pixel in each image over the crater in Fig. 9.

Fig. 11. Temperatures for the hot component (T_h) derived by dual-band analyses of the SWIR thermal anomalies, and the percentage of each pixel occupied by this component (f_h).

Table 1. Published observations of volcanic activity at Mt. Michael. *Cited in (Baker, 1990).

Table 2. Landsat parameters for top of atmosphere radiance calculation.

Table 3. Sentinel-2 parameter values for the two images analysed.

Table 4. ASTER gain values for conversion to radiance.

Table 5. MODTRAN generated transmissivities for each central wavelength.

Table 6. Summary of volcanic activity at Mt. Michael found through analysis of Landsat, ASTER and Sentinel-2 data, 1989-2018. *Pixel integrated temperatures acquired. **Dual-band analysis performed. +Thermal anomaly in TIR only.

Table 7. Pixel-integrated temperatures of the two SWIR bands for the warmest pixels over the crater of Mt Michael in Fig. 9.

Table 8. Summary of dual-band analysis from the five clear satellite images.

Date	Source/Mission	Observation
1820	Bellinghausen (Baker 1990)	Vapour emissions
1927, Jan	Capt. H Hansen, Kemp and Nelson (1932)	Vapour emissions
1930, 26 Feb	<i>RRS Discovery</i> , Kemp and Nelson (1932)	Vapour emissions
1937	<i>RRS William Scoresby</i> , Tyrell (1945)*	Vapour emissions
1952	<i>Hercules</i> , Secretaria de Marina (1958)*	Vapour emissions
1956	<i>HMS Protector</i> , Wilkinson (1957)*	Vapour emissions
1958	<i>General San Martín</i> , Secretaria de Marina (1958)*	Vapour emissions
1961	<i>Shackleton</i> , Turnbull (1961)*	Vapour emissions
1962	<i>HMS Protector</i> , Holdgate (1963)	Vapour emissions
1964, Mar	<i>HMS Protector</i> , Baker <i>et al</i> (1964)	Vapour emissions
1995	Lachlan-Cope <i>et al</i> (2001)	Plumes
1995, Mar	Lachlan-Cope <i>et al</i> (2001)	Thermal anomaly
1995, Jul	Lachlan-Cope <i>et al</i> (2001)	Thermal anomaly
1995, Sep	Lachlan-Cope <i>et al</i> (2001)	Thermal anomaly
1995, 11 Oct	Lachlan-Cope <i>et al</i> (2001)	Thermal anomaly
1996, Jan	Lachlan-Cope <i>et al</i> (2001)	Thermal anomaly
1996, Feb	Lachlan-Cope <i>et al</i> (2001)	Thermal anomaly
1996, 26 Mar	Lachlan-Cope <i>et al</i> (2001)	Thermal anomaly
1996, Apr	Lachlan-Cope <i>et al</i> (2001)	Thermal anomaly
1996, May	Lachlan-Cope <i>et al</i> (2001)	Thermal anomaly
1996, Aug	Lachlan-Cope <i>et al</i> (2001)	Thermal anomaly
1996, Sep	Lachlan-Cope <i>et al</i> (2001)	Thermal anomaly
1996, Oct	Lachlan-Cope <i>et al</i> (2001)	Thermal anomaly
1997, May	Lachlan-Cope <i>et al</i> (2001)	Thermal anomaly
1997, Aug	Lachlan-Cope <i>et al</i> (2001)	Thermal anomaly
1997, Sep	Lachlan-Cope <i>et al</i> (2001)	Thermal anomaly
1997, Oct	Lachlan-Cope <i>et al</i> (2001)	Thermal anomaly
2000	Patrick and Smellie (2013)	Thermal anomaly
2001	Patrick and Smellie (2013)	Thermal anomaly
2002	Patrick and Smellie (2013)	Thermal anomaly
2003	Patrick and Smellie (2013)	Thermal anomaly
2005	Patrick and Smellie (2013)	Thermal anomaly
2006	Patrick and Smellie (2013)	Thermal anomaly

Date	Source/Mission	Observation
2008	Patrick and Smellie (2013)	Thermal anomaly
2015, 28 Aug	MODIS, Global Volcanism Program (2018)	Thermal anomaly
2015, 30 Aug	MODIS, Global Volcanism Program (2018)	Thermal anomaly
2015, 31 Aug	MODIS, Global Volcanism Program (2018)	Thermal anomaly
2015, 30 Sep	MODIS, Global Volcanism Program (2018)	Thermal anomaly
2015, 2 Oct	MODIS, Global Volcanism Program (2018)	Thermal anomaly
2015, 6 Oct	MODIS, Global Volcanism Program (2018)	Thermal anomaly
2015, 6 Oct	MODIS, Global Volcanism Program (2018)	Thermal anomaly

Table 1. Published observations of volcanic activity at Mt. Michael. *Cited in Baker (1990).

Satellite	Acquisition date	M_L 1.65 μm	M_L 2.2 μm	A_L 1.65 μm	A_L 2.2 μm
Landsat 7	05.11.2003	0.12622	0.043898	-1.12622	-0.3939
Landsat 7	09.02.2004	0.12622	0.043898	-1.12622	-0.3939
Landsat 7	13.11.2006	0.12622	0.043898	-1.12622	-0.3939
Landsat 7	18.03.2006	0.12622	0.043898	-1.12622	-0.3939
Landsat 7	06.12.2011	0.12622	0.043898	-1.12622	-0.3939
Landsat 8	25.12.2015	0.00157	0.000530	-7.85945	-2.64906
Landsat 8	31.01.2018	0.00157	0.000528	-7.83203	0

Table 2. Landsat parameters for top of atmosphere radiance calculation.

Acquisition date	θ	$E_{e\lambda}$ 1.61 μm	$E_{e\lambda}$ 2.19 μm	U
10.02.2018	51.6	245.59	85.25	1.028335468
29.03.2018	68.66	245.59	85.25	1.005668623
03.04.2018	70.35	247.08	87.75	1.002796819

Table 3. Sentinel-2 parameter values for the images analysed.

Acquisition Date	Band 4 gain (1.65 μm)	Band 6 gain (2.205 μm)	Band 13 (TIR, μm)	Band 14 (TIR, μm)
13.07.2005	0.29	0.39	0.005693	0.005225
23.09.2005	0.2174	0.0625	0.005693	0.005225
28.10.2006	0.2174	0.0625	0.005693	0.005225
08.12.2006	0.2174	0.0625	0.005693	0.005225
02.11.2007	0.2174	0.0625	0.005693	0.005225

Table 4. ASTER gain values for conversion to radiance.

Atmospheric model	1.61 μm	1.65 μm	2.19 μm	2.2 μm
Sub-Arctic summer	0.881	0.933	0.890	0.924
Sub-Arctic winter	0.902	0.840	0.945	0.904
Average	0.892	0.887	0.918	0.914

Table 5. MODTRAN generated transmissivities for each central wavelength.

Date	Satellite	Activity	Date	Satellite	Activity	Date	Satellite	Activity
30/01/1989	Landsat 4	Eruption	29/11/2006	ASTER	Eruption	01/12/2015	ASTER	Plume
24/02/1989	Landsat 4	Volcanic clouds	08/12/2006*	ASTER	Possible lake	25/12/2015*	Landsat 7	Possible lava lake
29/04/1989	Landsat 4	Volcanic clouds	21/03/2007	ASTER	Plume	01/01/2016	Landsat 7	Volcanic clouds
06/03/1990	Landsat 4	Volcanic clouds	19/07/2007+	ASTER	TIR hotspot	08/01/2016	ASTER	Plume
22/03/1990	Landsat 4	Plume	02/11/2007*	ASTER	Possible lake	09/01/2016	ASTER	Plume
19/01/1999	Landsat 7	Volcanic clouds	02/11/2007	ASTER	Volcanic clouds	10/01/2016	Landsat 8	Volcanic clouds
13/05/2000	Landsat 7	Plume	18/11/2007	ASTER	Plume	18/01/2016	ASTER	Eruption
21/11/2000	Landsat 7	Volcanic clouds	25/11/2007	ASTER	Volcanic clouds	18/01/2016	ASTER	Eruption
01/01/2001	ASTER	Volcanic clouds	05/01/2008+	ASTER	TIR hotspot	27/07/2016	Landsat 8	Volcanic clouds
20/04/2001	ASTER	Eruption	25/01/2008	ASTER	Volcanic clouds	05/08/2016	Landsat 8	Volcanic clouds
20/01/2002	ASTER	Volcanic clouds	06/12/2008	ASTER	Plume	13/09/2016	Landsat 8	Plume
20/01/2002	ASTER	Volcanic clouds	20/12/2008	Landsat 7	Volcanic clouds	22/09/2016*	Landsat 8	Possible lava lake
03/02/2002	ASTER	Eruption	28/12/2008	ASTER	Eruption	29/09/2016	Landsat 8	Volcanic clouds
28/02/2002	Landsat 7	Volcanic clouds	10/03/2009	ASTER	Volcanic clouds	08/10/2016	Landsat 8	Plume
17/09/2002	ASTER	Volcanic clouds	25/08/2009+	ASTER	TIR hotspot	01/11/2016+	ASTER	TIR hotspot
29/10/2003	ASTER	Volcanic clouds	05/11/2009	ASTER	Eruption	01/11/2016	ASTER	Plume
05/11/2003*	Landsat 7	Possible lake	21/03/2010+	ASTER	TIR hotspot	08/11/2016	ASTER	Plume
23/11/2003	ASTER	Plume	19/08/2010+	ASTER	TIR hotspot	26/12/2016	ASTER	Plume
30/11/2003	Landsat 7	Plume	17/11/2010+	ASTER	TIR hotspot	08/03/2017	Landsat 8	Eruption
26/01/2004	ASTER	Volcanic clouds	19/12/2010	Landsat 7	Volcanic clouds	20/05/2017+	Landsat 8	TIR hotspot
26/01/2004	ASTER	Volcanic clouds	29/01/2011	ASTER	Volcanic clouds	23/07/2017	Landsat 8	Volcanic clouds
09/02/2004*	Landsat 7	Possible lake	29/01/2011	ASTER	Plume	02/10/2017	Landsat 8	Plume
16/11/2004	ASTER	Eruption	28/02/2011+	ASTER	TIR hotspot	03/11/2017	Landsat 8	Volcanic clouds
11/07/2005+	ASTER	TIR hotspot	16/03/2011	ASTER	Eruption	19/11/2017+	Landsat 8	TIR hotspot
13/07/2005**	ASTER	Possible lake	29/08/2011+	ASTER	TIR hotspot	28/11/2017	Landsat 8	Volcanic clouds
23/09/2005**	ASTER	Possible lake	04/11/2011	ASTER	Plume	29/11/2017	ASTER	Plume
03/11/2005	ASTER	Eruption	04/11/2011	ASTER	Plume	29/11/2017	ASTER	Eruption
12/11/2005	ASTER	Volcanic clouds	06/12/2011+	ASTER	TIR hotspot	22/12/2017	ASTER	Plume
29/01/2006	ASTER	Eruption	06/12/2011*	Landsat 7	Possible lake	29/12/2017	ASTER	Plume
07/02/2006	Landsat 7	Eruption	24/02/2012	Landsat 7	Eruption	31/01/2018**	Landsat 8	Possible lava lake
18/03/2006**	Landsat 7	Possible lake	27/04/2012+	ASTER	TIR hotspot	07/02/2018	Landsat 8	Plume
28/04/2006	Landsat 7	Eruption	15/11/2012	ASTER	Plume	10/02/2018*	Sentinel-2	Possible lava lake
14/07/2006+	ASTER	TIR hotspot	22/11/2012+	ASTER	TIR hotspot	29/03/2018**	Sentinel-2	Possible lava lake
24/08/2006	ASTER	Plume	01/12/2012+	ASTER	TIR hotspot	03/04/2018*	Sentinel-2	Possible lava lake
28/09/2006	ASTER	Plume	08/12/2012	Landsat 7	Plume	08/04/2018	Sentinel-2	Volcanic clouds
28/10/2006*	ASTER	Possible lake	17/06/2013+	ASTER	TIR hotspot	11/04/2018	Sentinel-2	Eruption
13/11/2006**	Landsat 7	Possible lake	16/11/2013	Landsat 7	Eruption	18/04/2018	Sentinel-2	Eruption
22/11/2006	ASTER	Eruption	12/11/2014	ASTER	Plume			
29/11/2006	Landsat 7	Eruption	05/01/2015	ASTER	Plume			

Table 6. Summary of volcanic activity at Mt. Michael found through analysis of Landsat, ASTER and Sentinel-2 data, 1989-2018. *Pixel integrated temperatures acquired. **Dual-band analysis performed. +Thermal anomaly in TIR only.

Date	Satellite	Pixel-Integrated Temperature, °C		
		1.61-1.65 μm	2.19-2.21 μm	Mean Temp.
05/11/2003	Landsat 7	416	252	334
09/02/2004	Landsat 7	397	228	312.5
13/07/2005	ASTER	331	237	284
23/09/2005	ASTER	393	292	342.5
18/03/2006	Landsat 7	339	247	293
28/10/2006	ASTER	468	292	380
13/11/2006	Landsat 7	434	274	354
08/12/2006	ASTER	444	270	357
02/11/2007	ASTER	384	231	307.5
06/12/2011	Landsat 7	434	274	354
25/12/2015	Landsat 8	422	248	335
31/01/2018	Landsat 8	505	333	419
10/02/2018	Sentinel-2	439	278	358.5
29/03/2018	Sentinel-2	570	376	473
03/04/2018	Sentinel-2	380	319	349.5

Table 7. Pixel-integrated temperatures of the two SWIR bands for the warmest pixels over the crater of Mt Michael in Fig. 9.

Satellite	Date	T_h (°C)	f_h %
ASTER	13/07/2005	989	0.38
ASTER	23/09/2005	1279	0.57
Landsat 7	18/03/2006	1259	0.03
Landsat 7	13/11/2006	1229	0.03
Landsat 8	31/01/2018	1200	0.17
Sentinel-2	10/02/2018	1228	0.17
Sentinel-2	29/03/2018	1040	0.24

Table 8. Summary of dual-band analysis from the five clear satellite images.

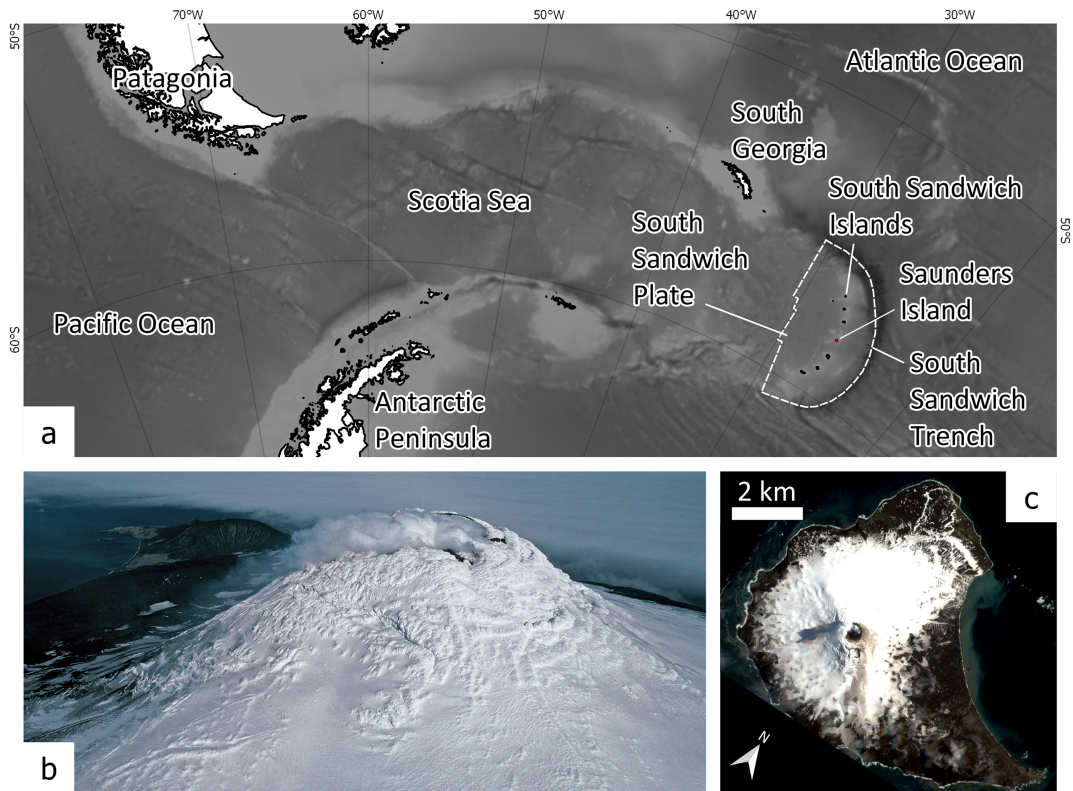


Figure 1

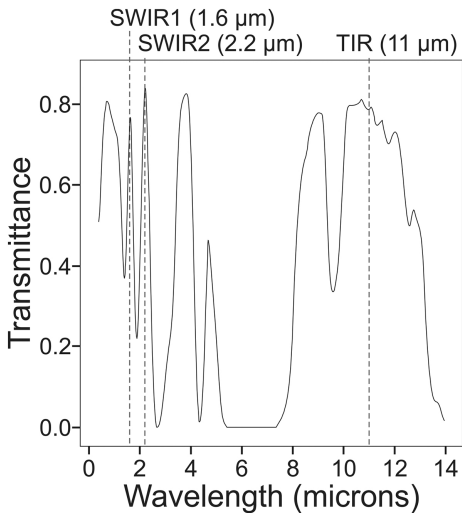


Figure 2

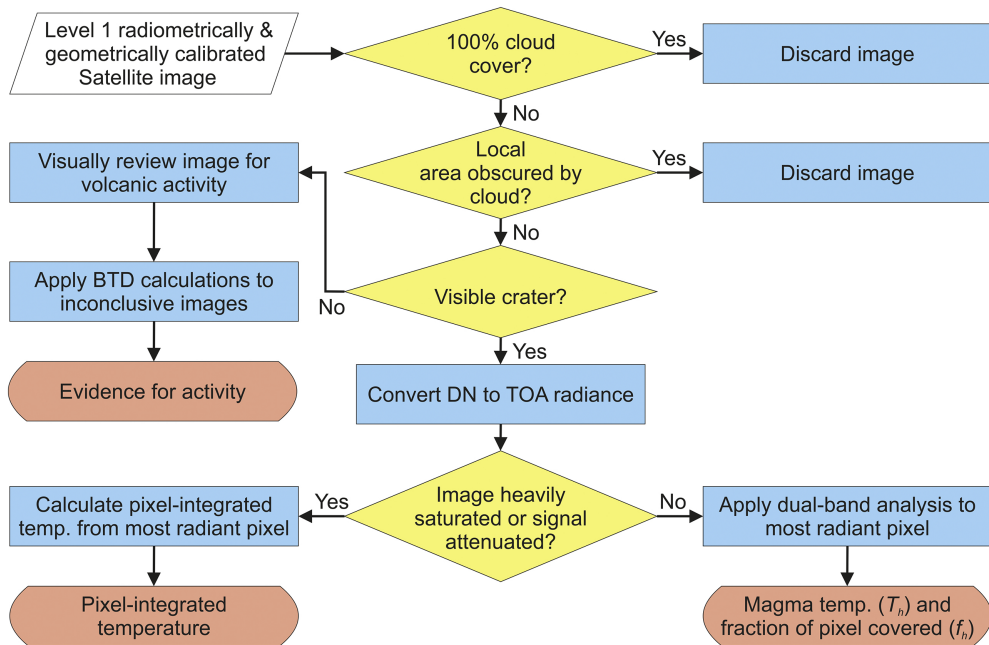


Figure 3

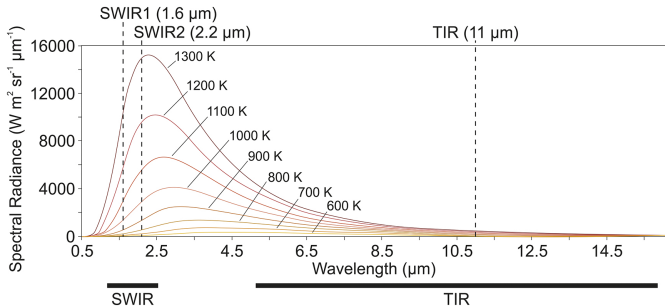


Figure 4

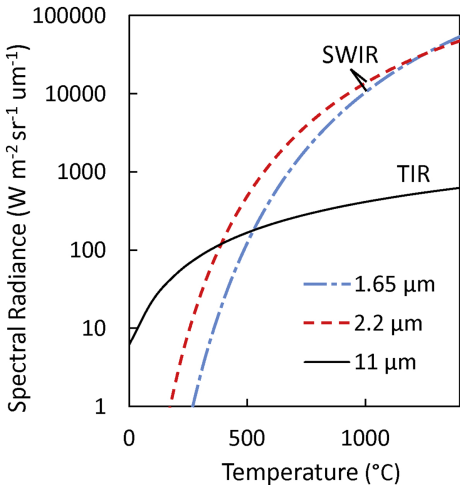


Figure 5

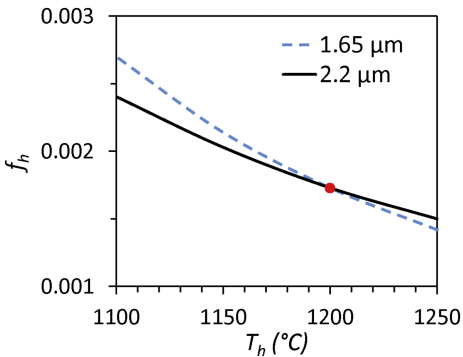


Figure 6

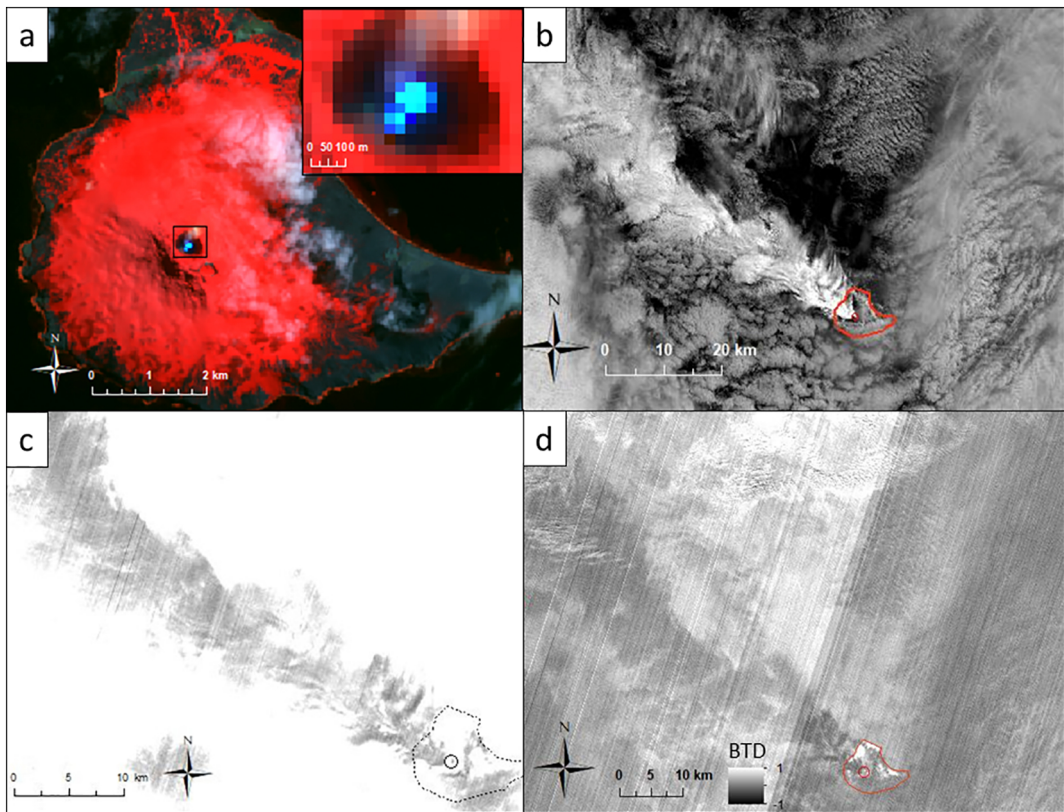


Figure 7

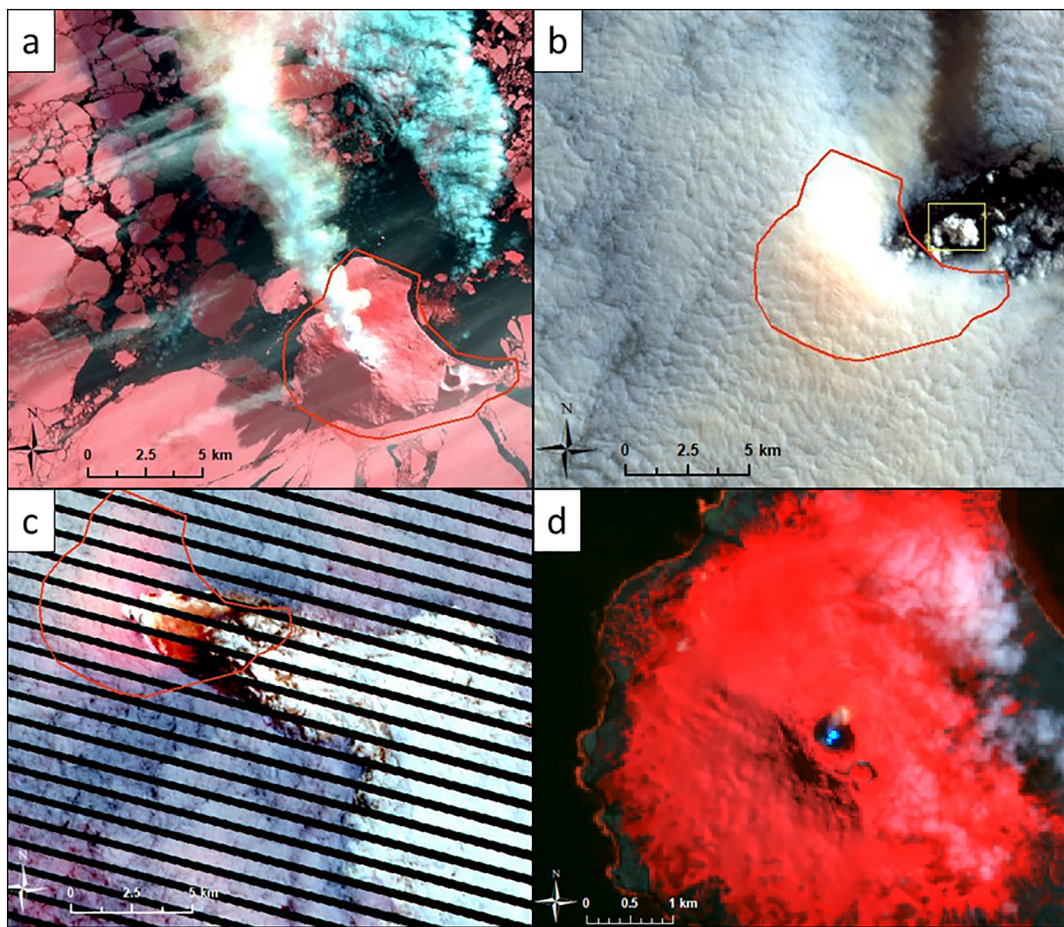


Figure 8

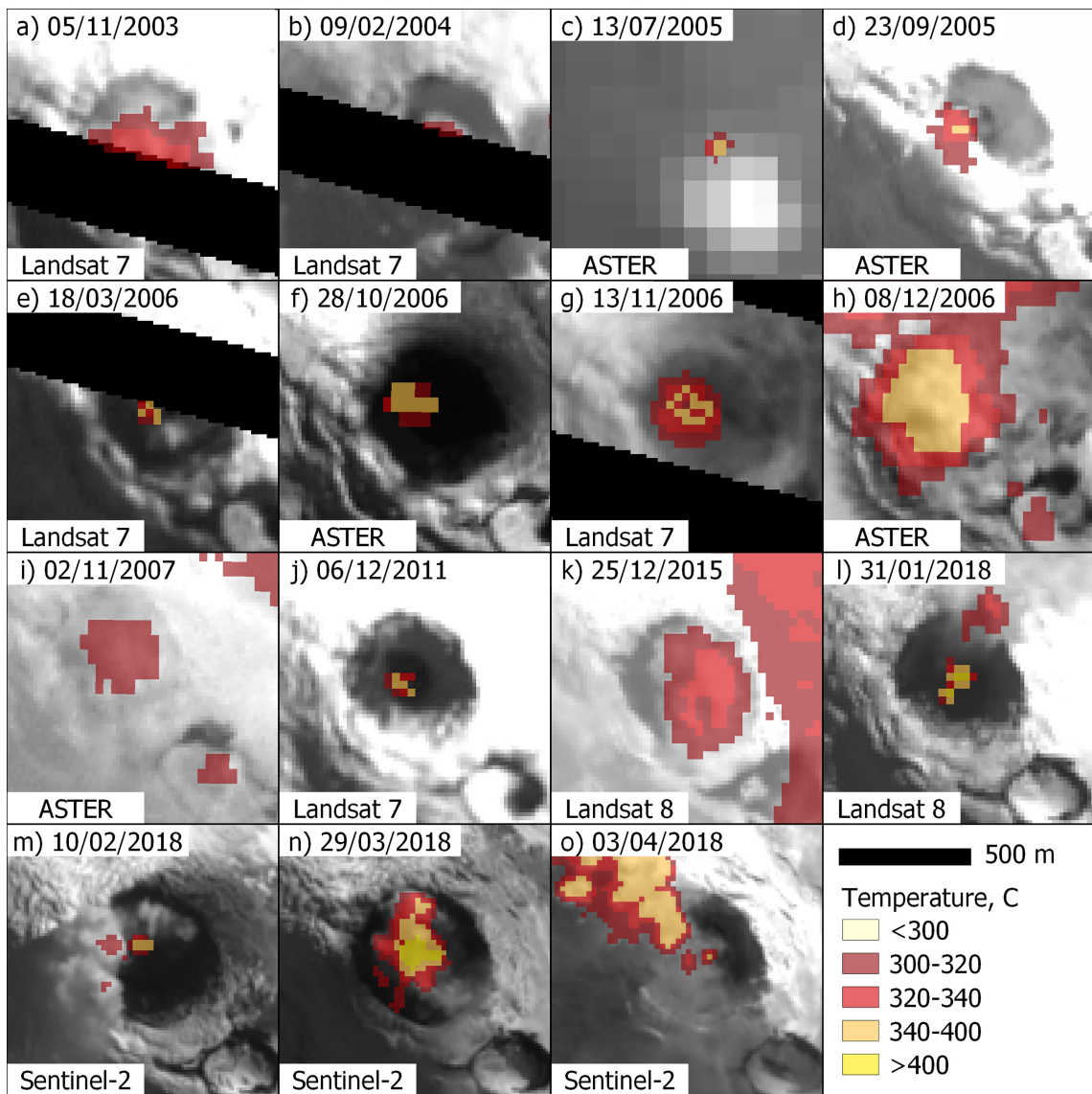


Figure 9

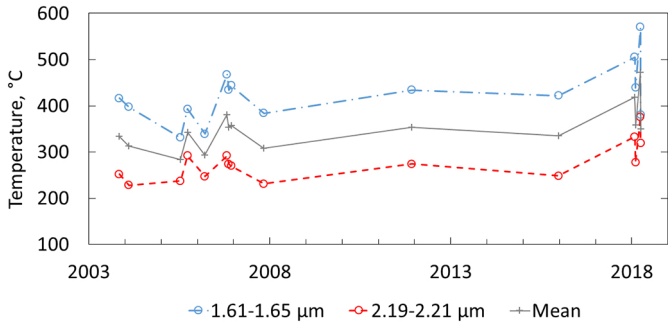


Figure 10

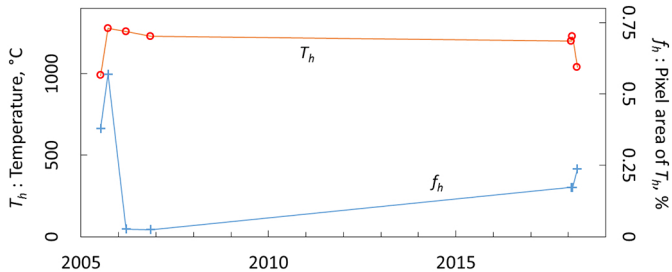


Figure 11